LOW FREQUENCY ELECTROMAGNETIC ENERGY HARVESTING FROM HIGHWAY BRIDGE VIBRATIONS

Michaël Peigney, Dominique Siegert

LOW FREQUENCY ELECTROMAGNETIC ENERGY HARVESTING FROM HIGHWAY BRIDGE VIBRATIONS

Michaël Peigney[1] and Dominique Siegert[2]

ABSTRACT

This paper focuses on energy harvesting from low frequency vibrations in bridges via an electromagnetic device. Two pre-stressed concrete highway bridges are considered as case studies. In situ vibration measurements are reported and analyzed. An electromagnetic Vibration Energy Harvester (VEH) with a low resonant frequency (tunable around 4Hz) has been designed. That VEH is of the cantilever type, with 12 magnets mounted on a beam and acting as an inertial mass. By electromagnetic induction, the moving magnets produce an electric current in a surrounding conductive coil. A single degree-of-freedom model of the VEH is presented with the main purpose of estimating the electrical power generated under various operating conditions. A procedure for identifying the model parameters from simple measurements is described. Optimizing the coil geometry so as to maximize the electromechanical coupling is crucial to maximize the output power. That issue does not seem to have been addressed in the literature and is discussed in detail in this paper. The coil that has been fabricated approximates that optimal geometry. For harmonic excitation with normalized amplitude, the designed VEH achieves the best power density to date among experimentally validated low-frequency electromagnetic VEHs. During a field test on a highway bridge, the harvester produced an average power of 112 μW through a load resistance of 3.3 kΩ. We present a simple formula for estimating the output power of electromagnetic VEHs in terms of traffic intensity. That formula could be useful in future studies related to vibration energy harvesting in bridges.

Keywords: energy harvesting, electromagnetic transduction, bridge vibrations, field test.

INTRODUCTION

Energy harvesting has become a very active research topic in recent years (Priya and Inman 2009). The overall idea is to convert ambient energy into electrical energy that can be used as a complement or an alternative to batteries for powering wireless devices. Ambient energy may exist in several forms, such as thermal, electromagnetic or vibrational. Energy harvesting from vibrations, which is addressed in this paper, relies on a transduction mechanism for converting kinetic energy into electric energy. The most frequently used ones are the piezoelectric, the electromagnetic and the electrostatic transduction mechanisms (Stephen 2006).

This paper focuses on energy harvesting from vibrations in bridges. Vibration Energy Harvesters (VEHs) are usually designed as resonant systems. For a maximum efficiency, the resonance frequency is usually tuned to match the main frequency of the vibrations in the host structure. The design of VEHs usually targets small scale devices with resonant

[1]Ph. D. Université Paris-Est, Laboratoire Navier (UMR 8205), CNRS, Ecole des Ponts ParisTech, IFSTTAR, F-77455 Marne la Vallée, France. Corresponding author, email: michael.peigney@polytechnique.org

[2]Ph. D. Université Paris-Est, IFSTTAR/COSYS, F-77455 Marne la Vallée, France.

frequencies above 30 Hz. Such high frequencies can be found in vibrations of machine tools, which are characterized by peak accelerations in the range of 1–10 m s^{-2} at frequencies between 70 and 120 Hz (Reilly et al. 2011). In contrast, bridge vibrations are characterized by low frequency (below 20 Hz) and small amplitude. Moreover, traffic-induced vibrations are non periodic. In such conditions, energy harvesting is a challenging issue.

Both theoretical and experimental work has been devoted to vibration energy harvesting in train bridges or highway bridges, mainly using piezoelectric materials (Ali et al. 2011; Peigney and Siegert 2013; Cahill et al. 2018), electromagnetic induction (Galchev et al. 2011; Kwon et al. 2013; Caruso et al. 2016) or a combination of both (Toyabur et al. 2018; Iqbal and Khan 2018). Although experimental investigations have been conducted, field tests remain relatively rare. Kwon et al. (2013) designed an electromagnetic VEH with a resonant frequency of 4.1 Hz and tested it on the 3$^{\mathrm{rd}}$ Nongro bridge located in a rural area in South Korea. An average power of 0.06 μW was obtained over the 10-second period corresponding to a heavy load truck crossing the bridge. The mean square acceleration measured on the bridge was 0.144 m.s^{-2}. Peigney and Siegert (2013) designed a piezoelectric VEH and tested it on a heavily trafficked highway bridge in France. That piezoelectric VEH was fixed on a water pipe which was acting as an auxiliary vibrating structure with a resonant frequency of 14.5 Hz. This paper aims at filling the gaps between existing field tests, by designing a VEH with a low resonant frequency and testing it on a highway bridge. One objective is to obtain representative values of the output power under real operating conditions.

Some vibration measurements carried out on 2 highway bridges are first reported. An electromagnetic VEH with a low resonant frequency has been designed for testing on a highway bridge. The designed VEH is of the cantilever type, with the magnets mounted on a beam and acting as an inertial mass. By electromagnetic induction, the moving magnets produce an electric current in a surrounding hand wound coil. A single degree-of-freedom model of the electromagnetic VEH is introduced for estimating the mean electrical power. In that model, the behavior of the VEH is captured by 5 parameters. The identification of those parameters from simple measurements is detailed.

It is well known that the electromechanical coupling coefficient should be as large as possible to maximize the efficiency of the VEH. Optimizing the coil geometry so as to maximize the electromechanical coupling is thus crucial. That issue does not seem to have been addressed in the literature and is discussed in detail in this paper. The coil that has been fabricated approximates that optimal geometry. Theoretical and experimental results on the mean electrical power that can produced by the considered VEH are presented. Laboratory tests are reported both for harmonic and non harmonic loadings. For harmonic loadings, the average output power P_m is proportional to the mass M and to the square of the RMS acceleration A_{rms}. The proposed device is shown to achieve the best P_m/MA_{rms}^2 ratio among experimentally validated low-frequency VEHs reported in the literature. We believe this is a consequence of the optimization of the electromechanical coupling.

Some results of a field test on a highway bridge are reported and compared with theoretical estimates. For designing VEHs fitted to bridge vibrations, it is desirable to have an explicit formula for the output power. Such a formula is not readily available for electromagnetic VEHs under traffic-induced excitations. The difficulty is that traffic-induced excitations are not harmonic in nature. By making use of the fact that traffic-induced excitations are sequence of random short-time pulses, we derive an explicit formula for estimating the output power of electromagnetic VEHs in terms of traffic intensity. That formula could be useful in future studies related to vibration energy harvesting in bridges.

MEASUREMENTS OF TRAFFIC-INDUCED VIBRATIONS IN A BRIDGE

A very common type of bridges on heavily trafficked highways was chosen as a vibration source for energy harvesting. A first case study is the Roberval bridge located in the north of France (A1 highway) and shown in Fig. 1. The superstructure including the bridge deck is composed of five braced girder beams made of prestressed concrete. The span length is 33 m.

As traffic induced vibrations depend on complex truck-bridge interactions involving random loading characteristics, vibration data were collected on site in service conditions. Acceleration in the vertical direction was measured with a capacitive accelerometer located at mid-span of the outer girder. The accelerometer used is a GCDC X2-2 data logger set-up at the high sensitivity mode with a $\pm$ 1.25 g range and a 15-bit analog digital converter. The selected sample frequency was 128 Hz. Two hours of measurements were recorded during a time in the day when the traffic intensity was high (before midday). As the mean interarrival time between lorries crossing the bridge at high speed was about 12 s, the vibration response recorded lasted enough time for assuming stationarity of the random process involving weights of vehicles, arrival times, suspension systems of the vehicles and surface irregularities.

A typical record of the acceleration signal is shown in Fig. 2. The root mean square acceleration was 3.4 10^{-2} m.s^{-2}. The related mechanical energy of vibration is mainly distributed among the first resonant frequencies of the bridge deck as shown in Fig. 3 where the mean power spectral density is displayed. The mean power spectral density of the measured acceleration was calculated with a frequency resolution of 0.02 Hz using the Welch's method implemented in Scilab, with 160 blocks of 5000 samples (Bunks et al. 2012). As can be observed in Fig. 3, two close resonant frequencies of the deck bridge are located at 4.1 Hz and 4.4 Hz in the spectrum. These frequencies are related to the first bending and torsion vibration modes of the superstructure (the terminology of the vibrations of a simply supported beam is adopted here). The resonant frequency at 14.5 Hz corresponds to the transverse bending mode. In Fig. 4 is shown the modal shape corresponding to the first bending mode, as obtained from a finite element calculation. The corresponding calculated frequency is 4 Hz. The frequencies provided by the finite element model for the next two relevant modes are 4.3 Hz and 15 Hz. Those values are relatively close to the experimental values (4.1, 4.4, 14.5 Hz). It can further be observed in Fig . 4 that the antinodes of the modes of vibration excited by the traffic are located at midspan of the outer girders beams.

As can be observed in Figs. 2 and 5(top), the acceleration signal is essentially a series of short-time pulses corresponding to lorries passing by. An example of an isolated pulse is shown in Fig. 6. Pulses are modulated periodic signals with an inner frequency about 4.1 Hz. The root mean square value of the peak acceleration of the pulses is about 0.11 m.s^{-2}.

A similar structure is also clearly observed on displacement measurements, see Fig. 5(bottom). The sample frequency was 100 Hz. In contrast with the acceleration signal, the pulses on the displacements are not modulated. Displacement measurements over a 2h30 period of time have been used to obtain statistics on the interarrival time between 2 consecutive pulses. The obtained histogram in shown in Fig. 7. In particular, the mean value of the interarrival time is 12.3 s.

Additional measurements were carried out on a similar highway bridge located in the south of France (Vareze bridge). For that bridge, the span length between the girder beams is 42 m. In Fig. 8 is shown a crossbraced girder beam of the Vareze bridge.

The mean power spectral density of the acceleration measured on the Vareze bridge is shown in Fig. 9. The root mean square acceleration was $3.6\ 10^{-2}$ m.s^{-2}, which is very close to the value obtained for the Roberval bridge. However, in contrast with the Roberval bridge, the power density is mainly concentrated at the first resonant frequency of the vibration modes of the bridge as can be observed in Fig. 9. It can also be observed that, as a result of the longer span length, the first resonant frequency (about 3 Hz) of the Vareze bridge is lower than that of the Roberval bridge.

DESIGN OF A RESONANT ELECTROMAGNETIC HARVESTER

A prototype cantilever-based electromagnetic harvester was designed for harvesting the low frequency traffic-induced vibrational energy of bridges. As low frequency and amplitude of movements were targeted, the proof mass of the inertial oscillator and the coil-permanent magnets arrangement were chosen for an effective electromechanical energy conversion. Although increasing the proof mass is beneficial for converting more mechanical energy into electrical energy, the experimental device had to be easily movable.

A global view of the device is shown in Fig 10. The main dimensions are indicated in Fig. 11. The two main components of the electromagnetic harvester are the magnetic circuit and the conductive coil, as shown in Figure 12. The magnetic circuit is composed of 12 permanent blocks magnets (neodynium grade N45). Each block magnet has dimensions $45 \times 30 \times 10$ mm and is magnetized through its width. The magnets are arranged on two ferromagnetic supports separated by an air gap of 8 mm. On each side of the air gap, the circuit hold two horizontal rows of 3 magnets with the same poling direction in the first row and opposite in the another one (Fig. 13). The poles of magnets facing through the air gap are the same, resulting in opposite magnetic fields in the upper and lower halves of the circuit. In Tables 1 and 2 are reported the locations and parameters of the magnets. The locations given in Table 1 are relative to an orthonormal frame with the x axis along the axis of the flat bar and the y axis along the bending direction. The magnetic circuit is supported by a cantilevered steel flat bar with cross section 2×45 mm^2 and a length of 35 cm from the clamped end. The total mass of the magnetic circuit, the cantilever steel bar and the coil is 2.4 kg.

The conductive coil is made of an enameled copper wire (diameter 0.5 mm) wounded on a rectangular PVC core (dimensions 120×13 mm) resulting in an approximate ellipse shape with the dimensions in the principal axis equal to 150 and 55 mm. The width of the coil is 4 mm.

Note that an additional movable mass was set on the the flat bar for tuning the resonant frequency of the mechanical oscillations. The electrical load resistance R_L was connected to the coil so as to adjust the electromagnetic damping.

MODELLING

Single degree of freefom model

The single mode approximation for the vibrations of the energy harvester powering a resistive load R_L leads to the equation of a single degree of freedom harmonic oscillator with viscous damping

$$m\ddot{y} + (c_m + \frac{K^2}{R_L + r_i})\dot{y} + ky = ma \tag{1}$$

where m is the modal mass related to the displacement y at the center of the coil, k is the stiffness of the cantilever beam, c_m is the mechanical damping, r_i is the resistance of the coil and a is the acceleration of the inertial base excitation (Elvin and Elvin 2011). In (1), K is the electromechanical coupling coefficient, giving the electromotive force voltage V in the coil as

$$V = K\dot{y} \tag{2}$$

The power P in the electrical load is

$$P = \frac{R_L}{(R_L + r_i)^2} K^2 \dot{y}^2 \tag{3}$$

Consider an harmonic base excitation $a(t) = A\cos\omega t$. The steady state response can be written as $y(t) = Re(Ye^{i\omega t})$ where

$$Y = H(\omega)A$$

and

$$H(\omega) = \frac{m}{k - m\omega^2 + i\omega(c_m + \frac{K^2}{R_L + r_i})} \tag{4}$$

It follows that the average power $\bar{P}$ in the electrical load is

$$\bar{P} = \frac{1}{2}\frac{R_L K^2}{(R_L + r_i)^2} |H(\omega)|^2 \omega^2 A^2$$

In particular, if the circular frequency ω of the excitation matches the natural circular frequency of the system $\omega_0 = \sqrt{k/m}$, the expression of the average power $\bar{P}$ becomes

$$\bar{P} = \frac{1}{2}\frac{R_L}{((R_L + r_i)c_m + K^2)^2} K^2 m^2 A^2 \tag{5}$$

For later reference, we record the maximum value of $\bar{P}$ in (5) that can be obtained from given parameters (K, r_i). That value, henceforth denoted by $\bar{P}(K, r_i)$, is obtained by maximizing (5) with respect to the load resistance R_L. Solving the equation $\partial\bar{P}/\partial R_L = 0$ gives the optimal load

$$R_L^{opt} = r_i + \frac{K^2}{c_m} \tag{6}$$

The relation (6) can be interpreted as a relation of resistance matching in the electrical domain (Stephen 2006). The impedance optimization in more general situations has been studied by Cai and Zhu (2020). A practical energy harvesting circuit that can be treated as an equivalent resistor is presented by Cai and Zhu (2019).

Substituting (6) in (5) gives

$$\bar{P}(K, r_i) = \frac{K^2 m^2}{8c_m(c_m r_i + K^2)} A^2 \tag{7}$$

Identification of the model parameters

The model has 5 parameters, namely r_i, m, k, c_m, K. The resistance of the coil r_i was measured with a Fluke multimeter model 80 series 5 and was found to be equal to 8 Ω. The other parameters were experimentally determined by measuring the displacement response in free vibration with a non-contact displacement transducer Micro-Epsilon NCDT 1302 and a digital acquisition card NI-9203. The mass distribution was first adjusted to tune the resonant frequency $\omega_0/2\pi$ to 4 Hz. The modal mass m was then derived from a small perturbation of the mass distribution by adding a mass Δm =78 g at the center of the magnetic circuit for inducing a change $\Delta\omega_0$ in the resonant frequency. We have indeed the relation (Clough and Penzien 1975)

$$m = -\frac{1}{2}\frac{\Delta m}{\Delta\omega_0}\omega_0$$

That procedure yielded a modal mass m equal to 1.9 kg. The stiffness k was deduced from ω_0 and m through the relation $k = m\omega_0^2$.

The procedure used for measuring the electromechanical coupling coefficient K and the mechanical damping c_m from free vibrations is now detailed. First note that Eq. (1) can be rewritten as $m\ddot{y} + C\dot{y} + ky = ma$ where the effective damping

$$C = c_m + \frac{K^2}{R_L + r_i} \tag{8}$$

is the sum of the mechanical dissipation c_m and of the electrical dissipation by Joule's effect in the resistance $R_L + r_i$. For a fixed value of R_L, the parameter C can be estimated using measurements of the free decays. Repeating the procedure for several values of R_L leads to experimental points marked as crosses in Fig. 14. The experimental results display an affine dependence between C and $(R_L + r_i)^{-1}$, in accordance with (8). The values of K and c_m have been obtained by performing a linear regression on the experimental results shown in Fig. 14.

All the values of the parameters of the model of the energy harvester are reported in Table 3. For those parameters, the optimal load resistance as given by (6) is 4.2 kΩ.

DESIGN OPTIMIZATION OF THE COIL

This section addresses the theoretical issue of finding the coil geometry that maximizes the performance of the VEH. The coil that has been fabricated approximates the optimal geometry as will be discussed.

Expression of the electromechanical coupling coefficient

First consider a single conductive loop $\Gamma(t)$ moving in a time-independent magnetic field $\boldsymbol{B}(\boldsymbol{x})$. The magnetic flux $\Phi(t)$ in the loop is given by

$$\Phi(t) = \int_{\Sigma(t)} \boldsymbol{B}(\boldsymbol{x}) \cdot \boldsymbol{n}\, dS \tag{9}$$

where $\Sigma(t)$ is the surface closed by $\Gamma(t)$ and $\boldsymbol{n}$ is the unit normal to $\Sigma(t)$. Assuming the loop to have a flat shape in the plane $(O, \boldsymbol{e}_x, \boldsymbol{e}_y)$ where $(O, \boldsymbol{e}_x, \boldsymbol{e}_y, \boldsymbol{e}_z)$ is an orthonormal frame, Eq. (9) becomes

$$\Phi(t) = \int_{\Sigma(t)} B_z(\boldsymbol{x})\, dS \tag{10}$$

with $B_z = \boldsymbol{B} \cdot \boldsymbol{e}_z$.

The motion of the loop is described by a transformation $(x, y, t) \mapsto F(x, y, t)$ which gives the location at time t of a material point initially located at $(x, y, 0)$. Considering only small rigid body motions in the plane $(O, \boldsymbol{e}_x, \boldsymbol{e}_y)$, the transformation F can be written as

$$F(x, y, t) = (x - \theta(t)\, y + X(t), \theta(t)\, x + y + Y(t), 0) \tag{11}$$

where $(X(t), Y(t))$ corresponds to a translation motion and $\theta(t)$ is an angle of rotation. Using (11), expression (10) for the magnetic flux can be rewritten as

$$\Phi(t) = \int_{\Sigma(0)} B_z(F(x, y, t))\, dS \tag{12}$$

Observing that the integration domain $\Sigma(0)$ is independent of time, we find

$$\frac{d\Phi(t)}{dt} = K_x \dot{X} + K_y \dot{Y} + K_\theta \dot{\theta} \tag{13}$$

with

$$\begin{aligned} K_x &= \int_{\Sigma(0)} \frac{\partial B_z}{\partial x}(x, y, 0) dS \\ K_y &= \int_{\Sigma(0)} \frac{\partial B_z}{\partial y}(x, y, 0) dS \\ K_\theta &= \int_{\Sigma(0)} -y \frac{\partial B_z}{\partial x}(x, y, 0) + x \frac{\partial B_z}{\partial y}(x, y, 0)\, dS \end{aligned} \tag{14}$$

In the following, we restrict our attention to loops that are *symmetric* with respect to the $\boldsymbol{e}_x$ and the $\boldsymbol{e}_y$ axis. We further assume that $B_z(x, -y, 0) = -B_z(x, y, 0) = -B_z(-x, y, 0)$ i.e. that the component B_z of the magnetic field (in the plane $(O, \boldsymbol{e}_x, \boldsymbol{e}_y)$) is *symmetric* with respect to the $\boldsymbol{e}_x$ axis and *antisymmetric* with respect to the $\boldsymbol{e}_y$ axis. In such case, it can easily be verified from expressions (14) that

$$K_x = K_\theta = 0$$

so that

$$\frac{d\Phi(t)}{dt} = K\dot{Y} \tag{15}$$

By Faraday's law of induction, the coefficient K identifies with the electromechanical coupling factor introduced in (2). Using (14) and Green's theorem, the coefficient K can be rewritten as

$$K = -\oint_{\Gamma(0)} B_z(x, y, 0) \boldsymbol{e}_x \cdot \boldsymbol{dl} \tag{16}$$

Shape optimization of the coil

In the following, attention is restricted to the situation where the magnetic field $\boldsymbol{B}$ is created by a set of N identical block magnets, as in the designed prototype. All the magnets are assumed to have a uniform magnetization oriented along $\boldsymbol{e}_z$. The magnetization in magnet i is denoted by $\varepsilon_i M \boldsymbol{e}_z$ where M is a constant (independent of i). We have

$$B_z(x, y, 0) = \sum_{i=1}^{N} \varepsilon_i B_z^0(x - x_i, y - y_i, -z_i) \tag{17}$$

where (x_i, y_i, z_i) is the center of magnet i and B_z^0 denotes the z component of the magnetic field created by a reference cubic magnet centered at O and having a uniform magnetization $M\boldsymbol{e}_z$. The calculation of B_z^0 is a classical problem of magnetostatics (Jackson 1975; Smythe 1988): We have

$$B_z^0(x, y, z) = \frac{\mu_0 M}{4\pi} \sum_{\epsilon_1, \epsilon_2, \epsilon_3 \in \{-1,1\}} \epsilon_1 \epsilon_2 \epsilon_3 \arctan \frac{(x - \epsilon_1 a_1)(y - \epsilon_2 a_2)}{(z - \epsilon_3 a_3) R} \tag{18}$$

where

$$R = \sqrt{(x - \epsilon_1 a_1)^2 + (y - \epsilon_2 a_2)^2 + (z - \epsilon_3 a_3)^2}$$

In (18), a_1, a_2 and a_3 are half the length of the magnet in the $\boldsymbol{e}_x$, $\boldsymbol{e}_y$ and $\boldsymbol{e}_z$ directions, respectively. The constant μ_0 is the vacuum permeability ($\mu_0 = 4\pi\, 10^{-7}$ H/m).

The map of B_z in the plane $(0, \boldsymbol{e}_x, \boldsymbol{e}_y)$ is shown in Fig. 15 for a set of 12 N45 magnets with properties listed in Tables 1 and 2. As can be observed in Fig. 15, B_z is almost piecewise constant in the plane $(0, \boldsymbol{e}_x, \boldsymbol{e}_y)$. In more detail, $B_z(x, y, 0)$ is almost zero outside of rectangular domains (of dimensions $2a_1 \times 2a_2$) that are the projections of the magnets on the $(0, \boldsymbol{e}_x, \boldsymbol{e}_y)$ plane. In each of the 3 rectangular domains located in the half-plane $y \geq 0$, the magnetic field B_z is almost uniform and equal to

$$B_0 = \frac{2\mu_0 M}{\pi} \sum_{\varepsilon \in \{-1,1\}} \varepsilon \arctan \frac{a_1 a_2}{(z_1 - \varepsilon a_3)\sqrt{(z_1 - \varepsilon a_3)^2 + a_1^2 + a_2^2}} \tag{19}$$

The formula (19) gives $B_0 \simeq 0.5$ T. In each of the 3 rectangular domains located in the half-plane $y \leq 0$, the magnetic field B_z is almost uniform and equal to $-B_0$. Note that the special distribution of the magnetic field observed in Fig. 15 results from the fact that the distance between the magnets and the plane $(0, \boldsymbol{e}_x, \boldsymbol{e}_y)$ is small.

The observation that B_z is (almost) piecewise constant allows for great simplification in the shape optimization of the loop. Denoting by $\mathcal{R}$ the set of rectangular domains in which B_z is non zero (Fig. 17), we have (as a first approximation)

$$K = -B^0 \int_{R \cap \Gamma(0)} \operatorname{sgn}(y)\, \boldsymbol{e}_x \cdot \boldsymbol{dl} \tag{20}$$

Using the Cauchy-Schwarz inequality, Eq. (20) implies that

$$K \leq 12 B^0 a_1 \tag{21}$$

Eq. (21) is satisfied as an equality for any loop such that $\mathcal{R} \cap \Gamma(0)$ is parallel to the $\boldsymbol{e}_x$ direction, as represented in Fig 16.

Consider now a planar coil (in the plane $(0, \boldsymbol{e}_x, \boldsymbol{e}_y)$) with N turns. Approximating each turn by a closed loop Γ_i, the flux $\Phi(t)$ in the coil satisfies the relation (15) with

$$K = -B^0 \sum_{i=1}^{N} \int_{R \cap \Gamma_i} \operatorname{sgn}(y)\, \boldsymbol{e}_x \cdot \boldsymbol{dl}$$

It follows that

$$K \leq 12 B^0 N a_1. \tag{22}$$

Consider a coil such that (22) holds as an equality, i.e. such $\mathcal{R} \cap \Gamma_i$ is parallel to the $\boldsymbol{e}_x$ direction, for all i. The maximum number N_{max} of turns in such a coil is $N_{max} = 2a_2/d$ where d is the diameter of the wire. Hence the maximum value of K that can be achieved by a planar coil is

$$K^{max} = 24\frac{B^0}{d}a_1a_2. \tag{23}$$

The formula (23) gives $K^{max} \simeq 8.1$ T.m. Among all the coils that satisfy $K = K^{max}$, the coil of minimal length as a rectangular shape as depicted in Fig 17. A simple calculation shows that the corresponding minimal length is

$$L \simeq \frac{2a_2}{d}(2a_2 + L_{\mathcal{R}})$$

where $L_{\mathcal{R}}$ is the length (in the $\boldsymbol{e}_x$ direction) of the rectangle bounded by $\mathcal{R}$ (see Fig. 17). For the data reported in Tables 1-2, we find $L \simeq 24$ m.

The formula (23) is approximate as it does not account for the variations of B_z at a fine length scale. For the rectangular coil shown in Fig. 17, a numerical calculation using the full expression (17) of the magnetic field gives $K \simeq 7.5$ T.m, which is about 10% smaller than the value obtained from (23).

Only planar coils have been considered so far, i.e. such that all the turns lie in the same plane. Larger values of K can be achieved by piling up turns in the $\boldsymbol{e}_z$ direction, as depicted in Fig 18. Let e be the height (in the $\boldsymbol{e}_z$ direction) of such a coil. In the optimal case of a compact packing (Fig. 18), the distance between 2 consecutive layers is $\sqrt{3}d/2$ and the number of layers M is approximatively $2e/(\sqrt{3}d)$. For a symmetric arrangement with respect to the plane $(0, \boldsymbol{e}_x, \boldsymbol{e}_y)$, the layer i is located in the plane $z = z_i$ with

$$z_i = \frac{e-d}{2}\left(-1 + 2\frac{i-1}{M-1}\right) \tag{24}$$

The coefficient K in such an arrangement can be written as

$$K = \sum_{i=1}^{M} K^i \tag{25}$$

where K^i is the coefficient obtained for a planar coil lying in the plane $z = z_i$. For instance, consider a rectangular coil of height $e = 4$mm in which each layer has the shape depicted in Fig 17. Combining (24) and (25) with the expression (17) of the magnetic field gives $K \simeq 68$ T.m. That value takes into account the variation of the magnetic field in the z direction. The length of the wire in that coil is approximatively equal to 216 m.

Approximation of the optimal coil

The coil of the prototype tested was designed in such fashion as to approximate the optimal geometry in Fig. 17. A perfectly rectangular coil as shown in Fig. 17 is difficult to achieve in practice, notably because of bending stiffness effects. Consecutive turns tend to become progressively rounder. In the designed coil, the first inner turn Γ_1 is almost rectangular with dimensions $2\tilde{a} \times 2\tilde{b}$ where $\tilde{a} = 120$ mm and $\tilde{b} = 6.5$ mm. The curve Γ_1 is thus defined by the equation

$$\max(|\frac{x}{\tilde{a}}|, |\frac{y}{\tilde{b}}|) \leq 1 \tag{26}$$

The outer turn Γ_N is almost elliptical with semi-axes $a = 150$ mm and $b = 55$ mm. The curve Γ_N is thus defined by the equation

$$\|(\frac{x}{a}, \frac{y}{b})\|_2 = \sqrt{\left(\frac{x}{a}\right)^2 + \left(\frac{y}{b}\right)^2} \leq 1 \tag{27}$$

As i increases from 1 to N, the turn Γ_i gradually changes from a rectangular shape to an elliptical shape. To model the shape of Γ_i, consider the α-norm $\|\cdot\|_\alpha$ in $\mathbb{R}^2$, defined for any $\alpha > 0$ by

$$\|(x, y)\|_\alpha = (|x|^\alpha + |y|^\alpha)^{1/\alpha}$$

A simple formula interpolating between (26) and (27) is

$$\|(\frac{x}{a(\alpha)}, \frac{y}{b(\alpha)})\|_\alpha \leq 1 \tag{28}$$

with

$$a(\alpha) = \tilde{a} + \frac{2}{\alpha}(a - \tilde{a}), b(\alpha) = b + \frac{2}{\alpha}(b - \tilde{b})$$

Eq. (26) defining Γ_1 and Eq. (27) defining Γ_N can indeed be put in the form (28) with $\alpha \to \infty$ and $\alpha = 2$, respectively. Similarly, we model Γ_i by using Eq. (28) for some value of α (denoted by α_i) to be determined, as is now explained: Let $l(\alpha)$ be the length of the curve defined by (28) and $S(\alpha)$ be the area of the surface bounded by that curve. Setting $\alpha(1) = \infty$, the parameter α_i is found in a sequential fashion by use of the relation

$$S(\alpha_{i+1}) = S(\alpha_i) + d\, l(\alpha_i) \tag{29}$$

where d is the diameter of the wire. The equation (29) is an approximate way of expressing the incompressibility of the wire. The coil geometry obtained from (29) is shown in Fig. 19 for a wire diameter d of 0.5 mm. The planar coil shown in Fig. 19 has 32 turns and a length L of approximatively 9.7 m.

The designed coil has a height of 4 mm. Assuming a compact packing has shown in Fig. 18, there are therefore 9 layers of wire in the $\boldsymbol{e}_z$ direction. Using the model geometry shown in Fig. 19 for each layer, the total length L and the coefficient K are found to be approximatively equal to 87 m and 34 T.m respectively.

We note that the length L is related to the resistance r_i of the coil through the relation

$$r_i = \frac{4\rho L}{\pi d^2} \tag{30}$$

Using the typical resistivity of copper ($\rho = 1.71\ 10^{-8}$ Ω.m), the resistance r_i of the coil predicted by (30) is 7.6 Ω which is in good agreement with the value measured experimentally (equal to 8 Ω, see Table 3). The value $K = 34$ T.m obtained from the model geometry of the coil is also in relatively good agreement with the value measured experimentally from free vibrations (equal to 30 T.m, see Table 3). The discrepancy between the theoretical and experimental values of K can be partly attributed to the idealization of the geometry, notably regarding the assumption of compact packing.

RESULTS

Experimental tests and numerical simulations were carried out to get estimates of the mean electric power converted in the optimal load resistance of the designed electromagnetic harvester.

Laboratory test

The harvester was first tested with an electrodynamic shaker LDS V650 as shown in Fig. 20. The harvester was connected to a load resistance $R_L = 4.2$ kΩ . The shaker was driven by an amplified harmonic voltage delivered by a waveform generator Agilent 33250A. The frequency was set to 4.1 Hz in order to match the resonant frequency of the energy harvester. Such a low value was below the usable frequency range (5 Hz - 4 kHz) of the shaker, resulting in an acceleration signal that was not perfectly harmonic. The measured acceleration after band pass filtering is shown in Fig.21, its root mean square value was A_{rms} =0.02 m.s^{-2}. In contrast with the excitation signal, the output voltage was found to be harmonic with a constant amplitude (Fig. 22). This results from the resonant nature of the VEH which acts as a narrow band pass filter. The mean electrical power in the load resistance was $P_m = A_{rms}^2/R_L$ =1.8 mW. Such a value is close to the theoretical value predicted by (7), which is equal to 1.7 mW for the excitation considered. This first test contributes to validate the model that has been presented previously.

The results for harmonic excitations can be used to compare the performance of the presented VEH with other devices from the literature. For an harmonic excitation, the average output power P_m is proportional to the mass M and to the square of the RMS acceleration A_{rms}. Experimental values of the ratio P_m/MA_{rms}^2 are reported in Table 4 for existing VEHs with low resonance frequency (below 5 Hz). The proposed device achieves a better P_m/MA_{rms}^2 ratio than existing low-frequency VEHs, which we believe is due to the optimization of the electromechanical coupling that has been carried out in the design of the presented VEH.

Field test

A test of the energy harvester was carried out on the bridge of Roberval. The device was set up at midspan of the outer girder beam. In Fig. 23 can be seen the energy harvester fixed on the superstructure as well as various equipments for measuring the bridge vibrations and the response of the energy harvester. In particular, the two dark green devices are GCDC X2-2 wireless accelerometers sensors, one being located at the clamped extremity of the cantilever (for measuring the base excitation) and the other being located on the VEH itself. Before installing the experimental device, the damping coefficient c_m was measured with the method of logarithmic decrement and found equal to 0.3 N.s.m^{-1}. The voltage measured at the output of the load resistance R_L=3.3 kΩ with a digital acquisition board NI USB6259 and is displayed in Fig. 24. The peak voltage was about 4 V. The experimental value of the mean electrical power was 112 μW. Those average values have been obtained over a testing time of approximately a 2 hours and a half around midday

It is interesting to compare that value with that predicted by the model. The theoretical value of the mean harvester power P is obtained by calculating the average power on the time interval $[-T/2, T/2]$ and taking the limit $T \to +\infty$, i.e.

$$P = \lim_{T\to+\infty} \frac{1}{T} \int_{-\infty}^{\infty} \frac{R_L}{(R_L + r_i)^2} K^2 \dot{y}_T^2 dt \tag{31}$$

where $y_T(t)$ is the displacement of the coil for the gated acceleration signal a_T defined as $a_T(t) = a(t)$ if $|t| \leq T/2$, and $a_T(t) = 0$ otherwise. Parseval's theorem allows (31) to be rewritten as

$$P = \lim_{T \to +\infty} \frac{1}{2\pi T} \int_{-\infty}^{\infty} \frac{R_L}{(R_L + r_i)^2} K^2 \omega^2 |\hat{y}_T(\omega)|^2 d\omega \tag{32}$$

where the superscript $\hat{}$ denotes the (non unitary) Fourier transform, e.g.

$$\hat{y}_T(\omega) = \int_{-\infty}^{+\infty} y_T(t) e^{-i\omega t} dt$$

Taking the Fourier transform of (1) shows that $\hat{y}_T(\omega) = H(\omega)\hat{a}_T(\omega)$ where $H(\omega)$ is defined as in (4). Hence (32) becomes

$$\bar{P} = \frac{1}{2\pi} \frac{R_L K^2}{(R_L + r_i)^2} \int_{-\infty}^{+\infty} |H(\omega)|^2 S_a(\omega) \omega^2 d\omega \tag{33}$$

where

$$S_a(\omega) = \lim_{T \to +\infty} \frac{|\hat{a}_T(\omega)|^2}{T} \tag{34}$$

is the power spectral density of the acceleration signal a as shown in Fig. 3. Eq. (33) yields a value of 97 μW, which is in reasonable agreement with the measured value. As in the laboratory test, we can observe that the theoretical value underestimates the experimental value. The theoretical value for the optimal value of 4.2 kΩ for the load resistance is 104 μW.

It is also interesting to compare the output power obtained with related results from field tests in the literature. In a previous study (Peigney and Siegert 2013), a piezoelectric energy harvester with a resonance frequency about 15 Hz was tested on the very same bridge. The mean electrical power generated was about 30 μW, which is significantly less than what is obtained with the presented electromagnetic harvester. Interestingly, those two energy harvesters target different (and well-separated) resonance frequencies and therefore can work cooperatively. Comparing the efficiency of different VEHs can be performed by calculating power densities, defined as the ratio of the average output over the mass of the VEH. To be fair, such a comparison should be done for VEHs submitted to similar excitations. (Kwon et al. 2013) tested a 56g-heavy VEH on a bridge with a main resonant frequency of 4 Hz (as in our case). The average energy during a single burst excitation (corresponding to an individual lorry passing by) was measured to be about 6 μW. The power density was thus about 105 μW/kg. The VEH presented in this paper weighs about 2.14 kg. The average power over a single burst excitation can obtained by dividing the power measured (112 μW) by the frequency of bursts (1/12.3 Hz) and the duration of a pulse (here taken as 6 s), giving 213 μ W. The obtained power density is thus about 320 μW/kg.

Additional predictions

Further investigations focus on extended predictions based on the model presented previously and the recorded acceleration responses measured during in-situ testing. Experimental power spectral estimates of the vibrations measured on the Roberval and Vareze bridges were used to this end.

In the case of Roberval bridge, the theoretical mean power estimate for the resonance at 15 Hz is only 39 μW. This result was obtained keeping the same effective mass, damping and electromagnetic conversion parameters for the harvester. The resonance frequency of the harvester was tuned to 15 Hz by changing only its effective stiffness.

In the case of Vareze bridge, the theoretical mean power estimate for the resonance at 3 Hz is about 500 μW. That value is again obtained by changing only the effective stiffness so as to tune the resonant frequency of the harvester to 3 Hz. The relatively high value obtained from the Vareze bridge stems from the fact that the vibration energy in the bridge is concentrated on a single peak (Fig. 9) instead of two close but distinct peaks as in the case of the Roberval bridge (Fig. 3).

Those results have been obtained under perfect tuning conditions: the resonance frequency of the harvester matches the targeted resonance frequency of the bridge. In real world applications, detuning effects are expected to come at play and need to be considered in the analysis. Even if perfectly tuned initially, the harvester may indeed detune due to external conditions. A related and perhaps more critical effect is the variation of the resonance frequencies of the bridge with the ambient temperature. The resonance frequencies of the bridge indeed decrease with the temperature. In a first approximation, that dependence is linear with a slope of 0.02 Hz per °C (Siegert et al. 2009). To put things in perspective, meteorological data collected over recent years show (MeteoFrance 2019) that the average monthly temperature on the bridge location vary between 4.2 °C and 18.5 °C. This corresponds approximatively to a 0.3 Hz variation of the resonant frequency (around 4.Hz).

In order to study the influence of detuning on the performance of the harvester, the mean electrical power was calculated for different values of the resonant frequency of the harvester (around 4 Hz). The results are shown in Fig. 25. The acceleration time record of the response of the Roberval bridge has been used in those calculations. As can observed in Fig. 25, the harvested electrical power is less than 50% of the maximum estimate when the tuning frequency is lower than 3.9 Hz or higher than 4.4 Hz.

A similar analysis has been done for the Vareze bridge. The corresponding results are shown in Fig. 26. For the Vareze bridge, the half power bandwidth is about 0.2 Hz and hence much smaller than in the case of the Roberval bridge. However, even for a relatively large detuning ($\pm$0.25 Hz), the output power predicted for the Vareze bridge remains larger than the maximum output power obtained for the Roberval bridge.

A simple formula for estimating the harvested power

As observed previously, traffic-induced excitations are essentially sequences of short-time pulses corresponding to individual lorries passing by. In a first approximation, each pulse is a modulated periodic signal with an inner circular frequency ω_i related to the modal frequencies of the bridge and the location of the harvester. Those observations can be used to obtain a simple model for relating the mean harvested power to traffic statistics. To this end, a pulse is here approximated by a function of the form

$$A\, f_0(t) \tag{35}$$

where

$$f_0(t) = \mathrm{tri}(t) \cos \omega_i t \tag{36}$$

and $\mathrm{tri}(t)$ is the triangle function defined as

$$\mathrm{tri}(t) = \begin{cases} 0 & \text{for } |t| > M \\ 1 + t/M & \text{for } - M \leq t \leq 0 \\ 1 - t/M & \text{for } 0 \leq t \leq M \end{cases} \tag{37}$$

The function f_0 is represented in Figure 27. In (35), the parameter M characterizes the duration of the pulse and A is the peak level. Consider a nonperiodic train of pulses

$$a(t) = \sum_{k=-\infty}^{+\infty} A_k f_0(t - t_k) \tag{38}$$

where A_k and t_k are random variables. Using brackets $\langle\ \rangle$ to denote ensemble averages, we obtain from (33) that

$$\langle \bar{P} \rangle = \frac{1}{2\pi} \int_{-\infty}^{\infty} \frac{R_L}{(R_L + r_i)^2} K^2 \omega^2 S_a(\omega) |H(\omega)|^2 d\omega \tag{39}$$

where $S_a(\omega)$ is now defined by

$$S_a(\omega) = \lim_{T \to +\infty} \frac{\langle |\hat{a}_T(\omega)|^2 \rangle}{T} \tag{40}$$

We refer to the textbooks of Drake (1967) and Mix (1995) for more details on random signal theory. Assuming that pulse emission events are independent, the spectral density S_a of a random train of pulses (38) can be calculated using Carson's theorem (Carson 1931; Mix 1995), giving

$$S_a(\omega) = N \langle A^2 \rangle |\hat{f}_0(\omega)|^2 + 2\pi \delta(\omega) \left[N \langle A \rangle \int_{\infty}^{+\infty} f_0(t) dt \right]^2 \tag{41}$$

where N is the average rate of pulse emission and δ is the Dirac distribution. Substituting (41) in (39) yields

$$\langle \bar{P} \rangle = N \langle A^2 \rangle E_0 \tag{42}$$

where

$$E_0 = \frac{1}{2\pi} \frac{R_L}{(R_L + r_i)^2} K^2 \int_{-\infty}^{+\infty} |\hat{f}_0(\omega)|^2 |H(\omega)|^2 \omega^2 d\omega \tag{43}$$

It can be calculated from (36) that

$$|\hat{f}_0(\omega)|^2 = \frac{M^2}{4} \left(\mathrm{sinc}^2 \frac{M(\omega_i + \omega)}{2} + \mathrm{sinc}^2 \frac{M(\omega_i - \omega)}{2} \right)^2$$

Using the model parameters reported in (3) and taking $\omega_i/2\pi = 4.1$ Hz, $c_m = 0.3$ N.m.s^{-1}, R_L= 3.3 kΩ, the energy E_0 in (43) is equal to 0.106 J. As reported previously, the root mean square value $\sqrt{\langle A^2 \rangle}$ of the peak acceleration is 0.11 m.s^{-2} for the Roberval bridge. The mean value of the interarrival time between two pulses is 12.3 s, hence the average rate of pulse emission N is equal to 1/12.3 Hz. Using those values, formula (42) yields $\langle \bar{P} \rangle = 105$ μW, which is quite close to the measured value (112 μW). Eq. (42) is approximate but is of very simple use. It allows one to estimate the harvested energy in terms of traffic intensity.

CONCLUSION

The designed electromagnetic VEH targets the first bending and vibration modes of the highway bridges considered. The corresponding frequency are about 4Hz and the root mean square acceleration is about 3.5 10^{-2} m.s^{-2}. The chosen coil geometry as be chosen in such fashion to optimize the electromechanical coupling. During field test, the electrical power generated by the VEH was 112 μW with a peak voltage of 4 V. That average power was obtained over approximatively 2 h 30 min of field testing. A single degree-of-freedom model with 5 parameters has been presented. That model allows to get approximate but simple estimates of the output power under various operating conditions. In particular, values up to 500 μW are expected to be obtained on the Vareze bridge for which the vibration energy is concentrated on a single peak.

In the context of structural health monitoring, the harvested energy could be used to power wireless sensor nodes. To put things in perspective, it has been shown in (Reilly et al. 2011) that a wireless acceleration sensor transmitting every 10 seconds requires a power of 3 mW. Cross multiplication suggests that the power generated by the presented VEH on the Roberval bridge (112 μW) could be used for feeding a wireless sensor transmitting every 5 minutes or so, which could be relevant for slow time varying quantities such as temperature, humidity or air pollution.

It would be interesting to go further in that direction by combining the designed electromagnetic VEH with a power conditioning circuit and a dedicated sensor with low duty cycle. Future work will focus on improving the performance of the device. In that regard, other pole arrangements could be considered. For electromagnetic dampers, it was indeed found that the energy density could be improved by considering several rows of magnets with alternated poles (Zuo et al. 2011). In this paper, we used two rows of magnets but considering additional rows would possibly be helpful in improving the electromechanical coupling. The shape and arrangements of the coils should be optimized accordingly. Another possible strategy for improving the performance of the device is to make use of nonlinear phenomena such a bistability (Harne and Wang 2013), impact (Cottone et al. 2014) or parametric resonance (Mam et al. 2017).

DATA AVAILABILITY

Data, models, and Matlab code generated during the study are available from the corresponding author by request.

ACKNOWLEDGEMENTS

The authors thank Roland Vidal (SNCF), Amer Abouzeid (Sixense), Xavier Chapeleau (IFSTTAR) and Erick Merliot (IFSTTAR) for their help.

APPENDIX I. REFERENCES

Ali, S., Friswell, M., and Adhikari, S. (2011). "Analysis of energy harvesters for highway bridges." *Journal of Intelligent Material Systems and Structures*, 22(16), 1929–1938.

Bunks, C., Chancelier, J.-P., Delebecque, F., Goursat, M., Nikoukhah, R., and Steer, S. (2012). *Engineering and scientific computing with Scilab*. Springer Science & Business Media.

Cahill, P., Mathewson, A., and Pakrashi, V. (2018). "Experimental validation of piezoelectric energy-harvesting device for built infrastructure applications." *Journal of Bridge Engineering*, 23(8), 04018056.

Cai, Q. and Zhu, S. (2019). "Enhancing the performance of electromagnetic damper cum energy harvester using microcontroller: Concept and experiment validation." *Mechanical Systems and Signal Processing*, 134, 106339.

Cai, Q. and Zhu, S. (2020). "Unified strategy for overall impedance optimization in vibration-based electromagnetic energy harvesters." *International Journal of Mechanical Sciences*, 165, 105198.

Carson, J. R. (1931). "The statistical energy-frequency spectrum of random disturbances." *Bell System Technical Journal*, 10(3), 374–381.

Caruso, G., Chirianni, G., and Vairo, G. (2016). "Energy harvesting from wind-induced bridge vibrations via electromagnetic transduction." *Engineering Structures*, 115, 118–128.

Clough, R. W. and Penzien, J. (1975). "Structural dynamics." *McGrawHill Inc, New York zbMATH*.

Cottone, F., Frizzell, R., Goyal, S., Kelly, G., and Punch, J. (2014). "Enhanced vibrational energy harvester based on velocity amplification." *Journal of Intelligent Material Systems and Structures*, 25(4), 443–451.

Drake, A. W. (1967). *Fundamentals of applied probability theory*. Mac Graw Hill.

Elvin, N. G. and Elvin, A. A. (2011). "An experimentally validated electromagnetic energy harvester." *Journal of Sound and Vibration*, 330(10), 2314–2324.

Galchev, T., McCullagh, J., Peterson, R., and Najafi, K. (2011). "Harvesting traffic-induced vibrations for structural health monitoring of bridges." *Journal of Micromechanics and Microengineering*, 21(10), 104005.

Harne, R. and Wang, K. (2013). "A review of the recent research on vibration energy harvesting via bistable systems." *Smart materials and structures*, 22(2), 023001.

Iqbal, M. and Khan, F. U. (2018). "Hybrid vibration and wind energy harvesting using combined piezoelectric and electromagnetic conversion for bridge health monitoring applications." *Energy Conversion and Management*, 172, 611–618.

Jackson, J. D. (1975). *Classical electrodynamics*. John Wiley & Sons.

Jung, H.-J., Kim, I.-H., and Jang, S.-J. (2011). "An energy harvesting system using the wind-induced vibration of a stay cable for powering a wireless sensor node." *Smart materials and structures*, 20, 075001.

Kwon, S.-D., Park, J., and Law, K. (2013). "Electromagnetic energy harvester with repulsively stacked multilayer magnets for low frequency vibrations." *Smart materials and structures*, 22(5), 055007.

Mam, K., Peigney, M., and Siegert, D. (2017). "Finite strain effects in piezoelectric energy harvesters under direct and parametric excitations." *Journal of Sound and Vibration*, 389, 411–437.

MeteoFrance (2019). "Public data, <https://donneespubliques.meteofrance.fr>.

Mix, D. F. (1995). *Random signal processing*. Prentice-Hall, Inc.

Peigney, M. and Siegert, D. (2013). "Piezoelectric energy harvesting from traffic-induced bridge vibrations." *Smart Materials and Structures*, 22(9), 095019.

Priya, S. and Inman, D. J. (2009). *Energy harvesting technologies*, Vol. 21. Springer.

Reilly, E. K., Burghardt, F., Fain, R., and Wright, P. (2011). "Powering a wireless sensor node with a vibration-driven piezoelectric energy harvester." *Smart materials and structures*, 20(12), 125006.

Siegert, D., Mevel, L., Reynders, E., De Roeck, G., and Goursat, M. (2009). "Variation of modal parameter estimates of a prestressed concrete bridge." *27th International Modal Analysis Conference (IMAC-XXVII)*.

Smythe, W. B. (1988). *Static and dynamic electricity*. Hemisphere publishing.

Stephen, N. G. (2006). "On energy harvesting from ambient vibration." *Journal of sound and vibration*, 293(1-2), 409–425.

Toyabur, R., Salauddin, M., Cho, H., and Park, J. Y. (2018). "A multimodal hybrid energy harvester based on piezoelectric-electromagnetic mechanisms for low-frequency ambient vibrations." *Energy Conversion and Management*, 168, 454–466.

Zuo, L., Chen, X., and Nayfeh, S. (2011). "Design and analysis of a new type of electromagnetic damper with increased energy density." *Journal of vibration and acoustics*, 133(4), 041006.

TABLE 1. Locations and orientations of the magnets

i	x_i (mm)	y_i (mm)	z_i (mm)	ϵ_i
1	-47.5	17.5	9	-1
2	0	17.5	9	-1
3	47.5	17.5	9	-1
4	-47.5	-17.5	9	1
5	0	-17.5	9	1
6	47.5	-17.5	9	1
7	-47.5	17.5	-9	-1
8	0	17.5	-9	-1
9	47.5	17.5	-9	-1
10	-47.5	-17.5	-9	1
11	0	-17.5	-9	1
12	47.5	-17.5	-9	1

TABLE 2. Parameters of the magnets

a_1 (mm)	a_2 (mm)	a_3 (mm)	$\mu_0 M$ (T)
22.5	15	5	1.32

TABLE 3. Estimated values of the parameters of the electromagnetic harvester.

m (kg)	k (N·m^{-1})	c_m (N·s·m^{-1})	K (T·m)	r_i (Ω)
1.9	1260	0.22	30.3	8

TABLE 4. Experimental results for harmonic excitations on low-frequency VEHs

Power P_m (mW)	Frequency (Hz)	Mass M (g)	RMS Acceleration A_{rms} (m.s^{-2})	Ratio P_m/MA_{rms}^2 (mW/g.m.s^{-2})	Reference
27.14	2.8	171	0.748	0.039	(Jung et al. 2011)
0.118	3.7	56	0.25	0.104	(Kwon et al. 2013)
1.8	4.1	2400	0.02	6.761	presented device

List of Figures

FIG. 1. Roberval bridge and view of its superstructure.

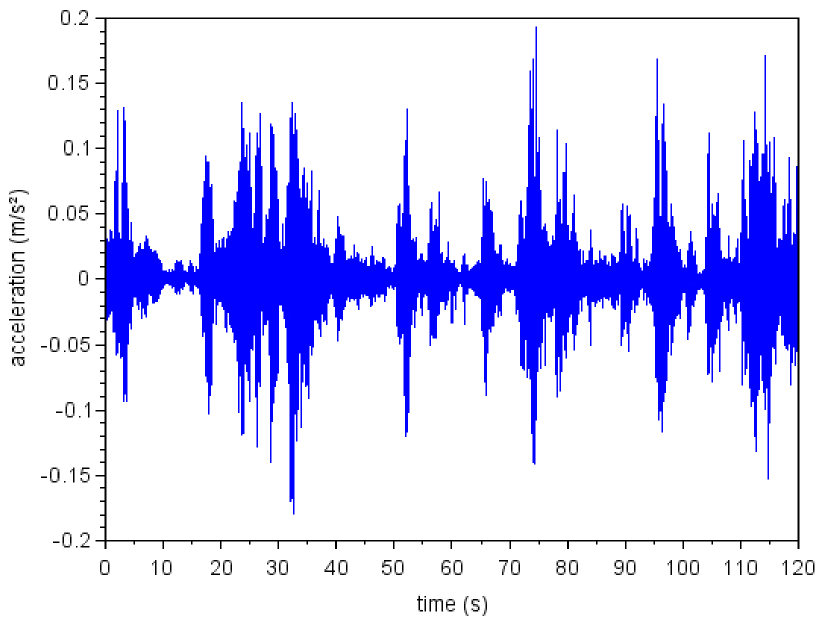

FIG. 2. Sample of the time history acceleration response.

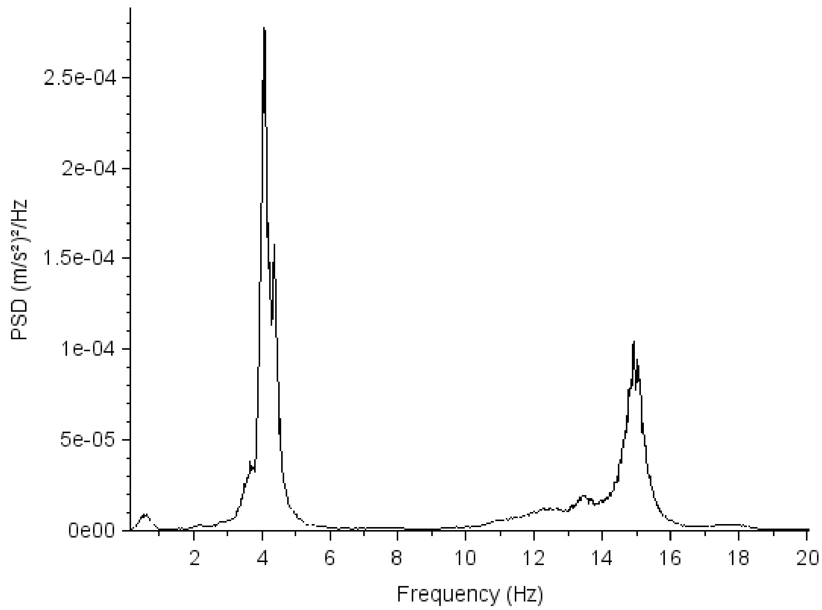

FIG. 3. Mean power spectral density of the measured acceleration on the Roberval bridge.

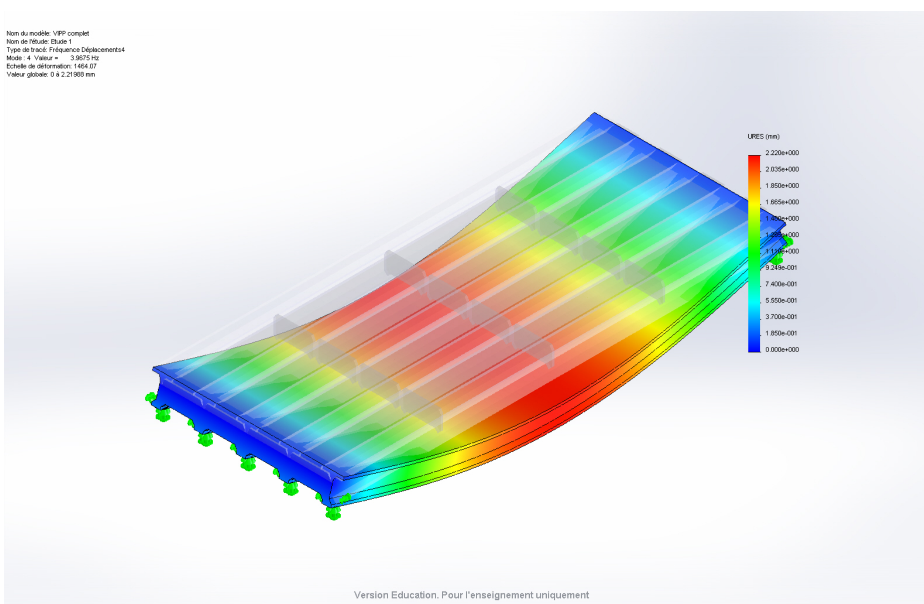

FIG. 4. Modal shape of the first bending mode of the bridge.

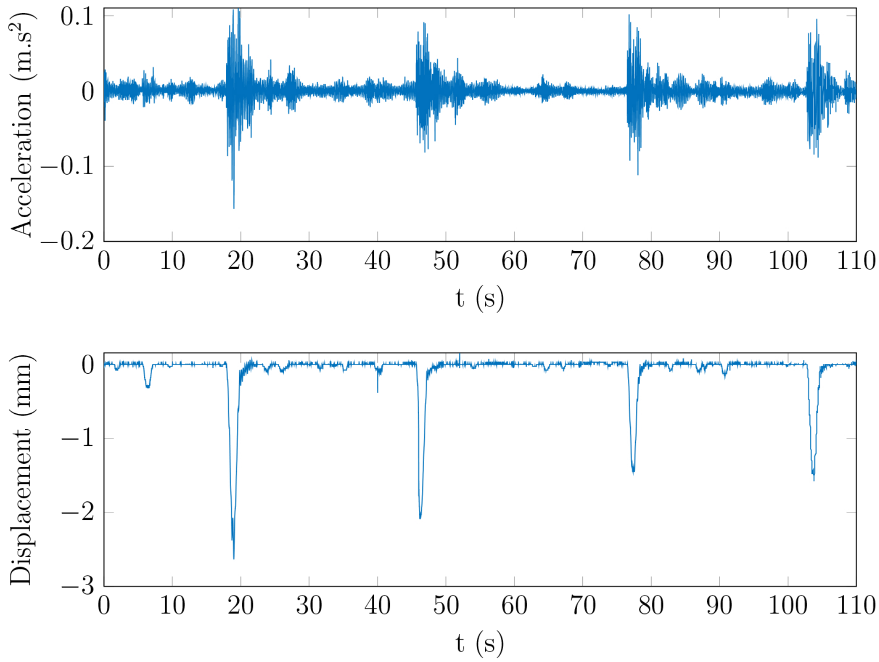

FIG. 5. Synchronized measurements of the acceleration (top) and displacement (bottom).

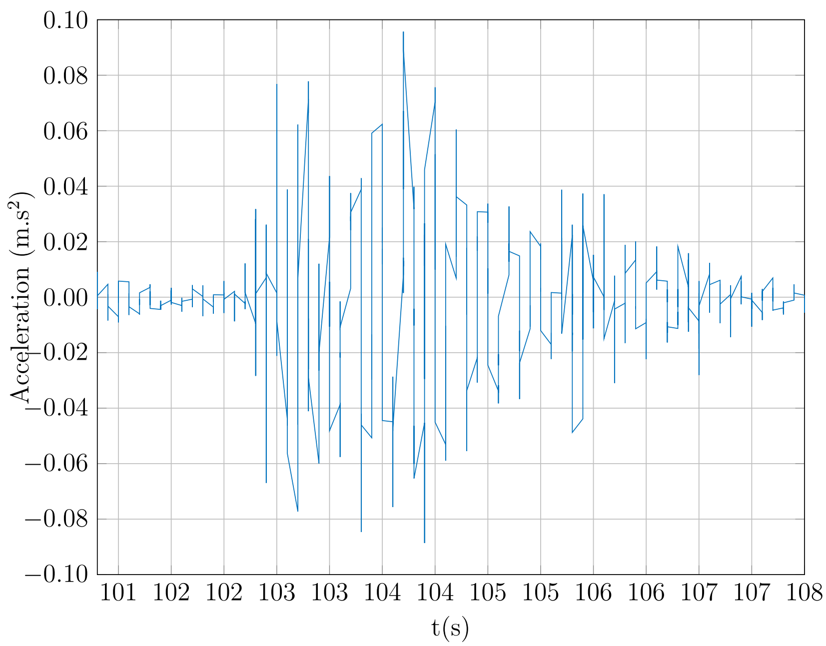

FIG. 6. Example of a pulse in the acceleration signal.

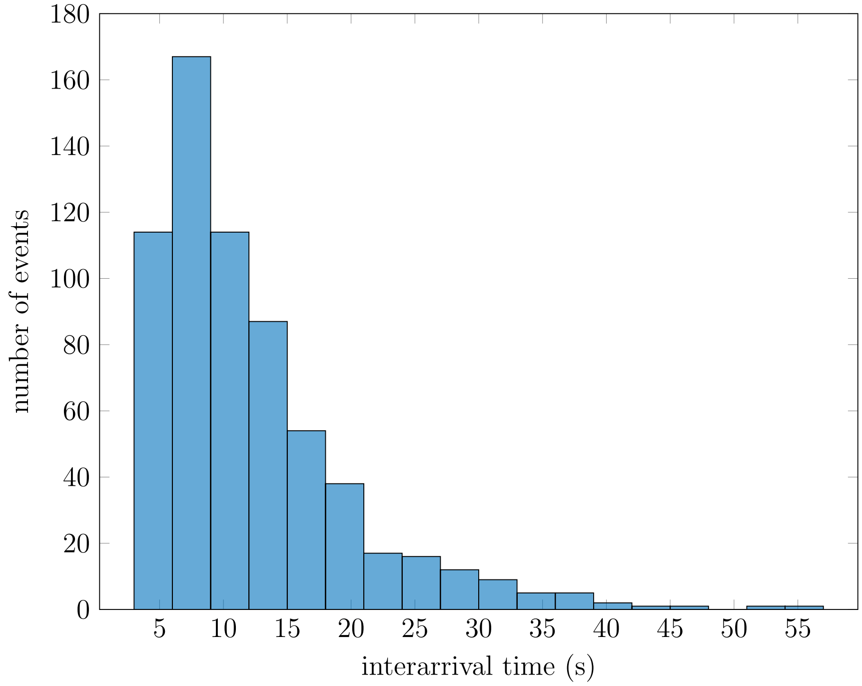

FIG. 7. Histogram of the interarrival time

FIG. 8. Girder beam of the Vareze bridge.

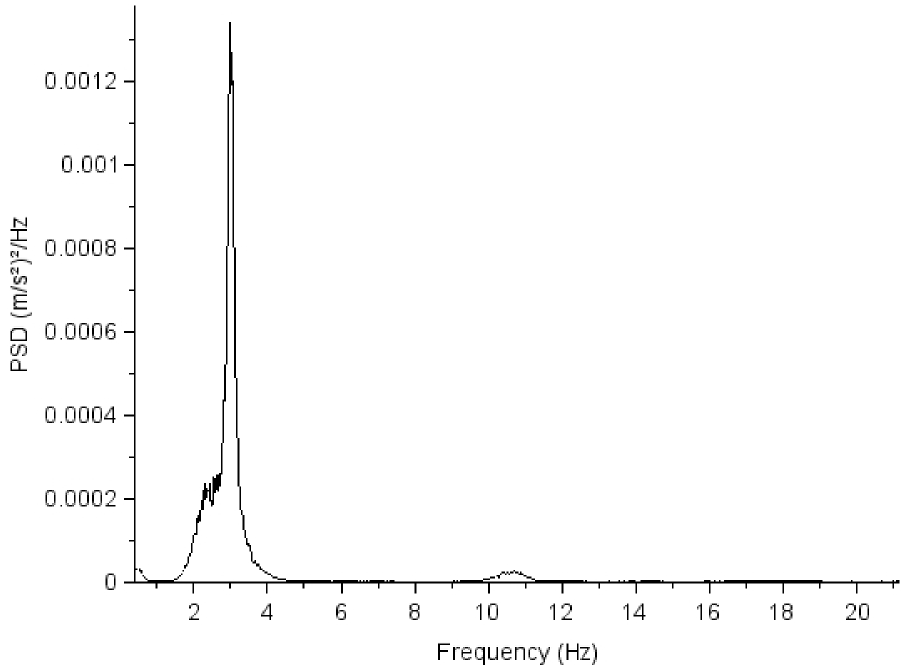

FIG. 9. Mean power spectral density of the measured acceleration on the Vareze bridge.

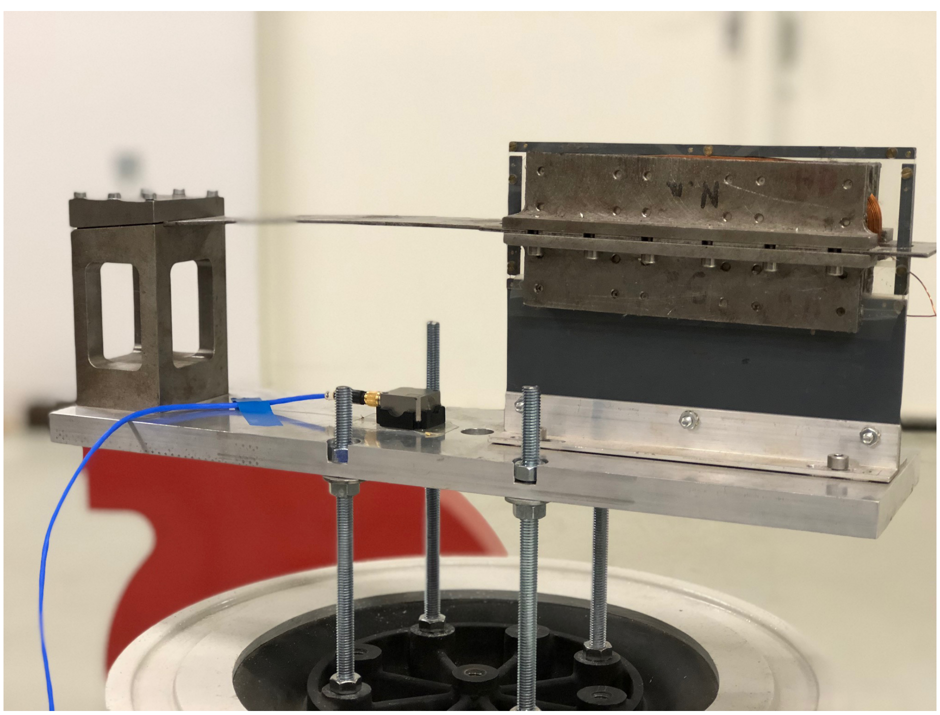

FIG. 10. Electromagnetic harvester.

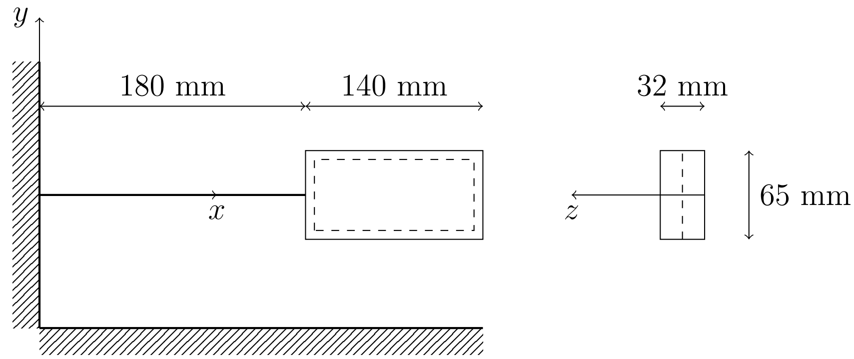

FIG. 11. Dimensions of the VEH (side and front views).

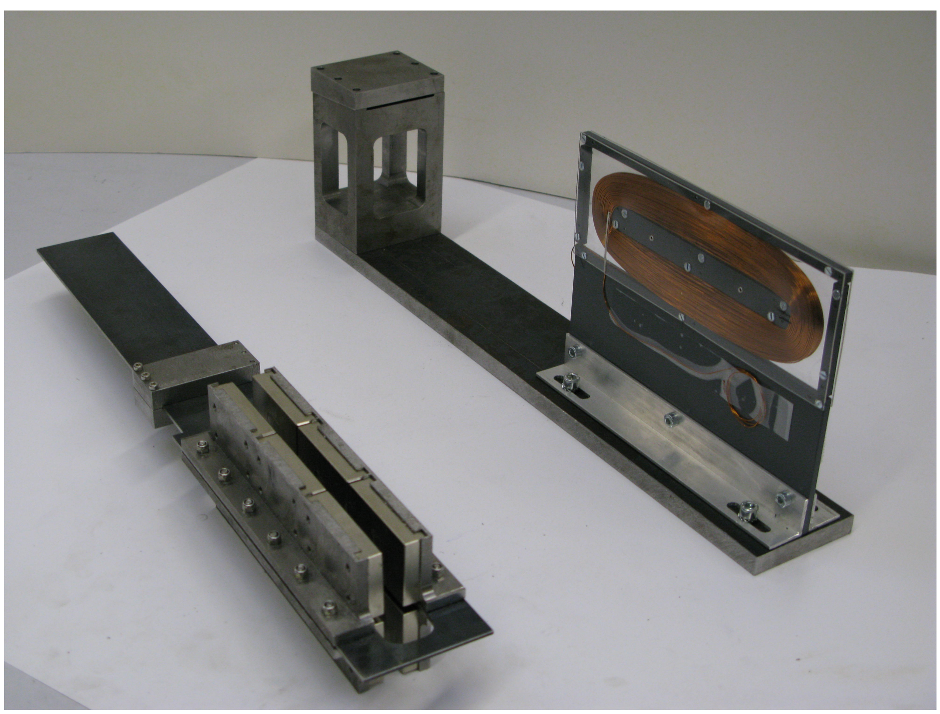

FIG. 12. The two main components of the electromagnetic harvester.

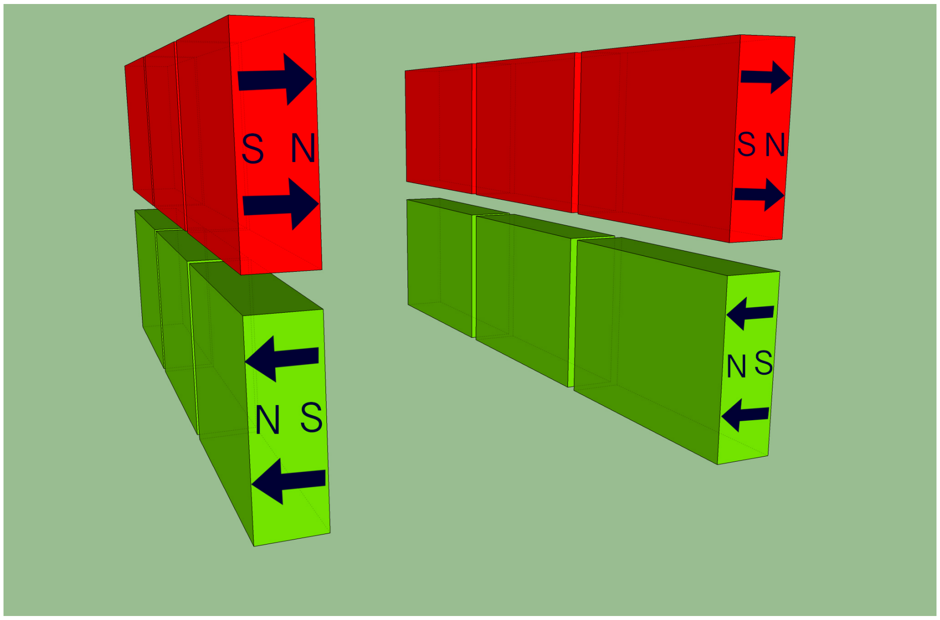

FIG. 13. Magnetic circuit (the gap in the z direction is exaggerated for better clarity). Magnets of the same color have the same magnetization.

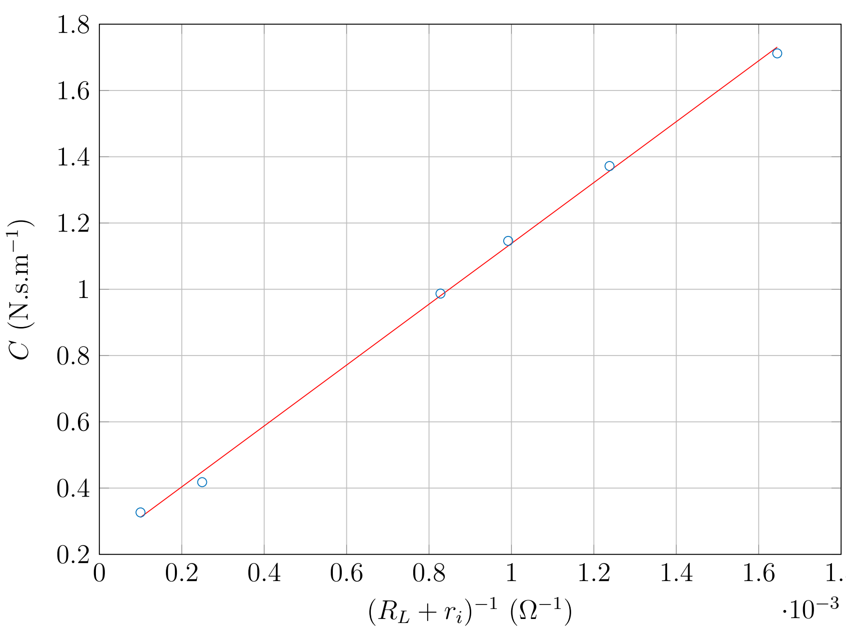

FIG. 14. Least squared identification of K and c_m.

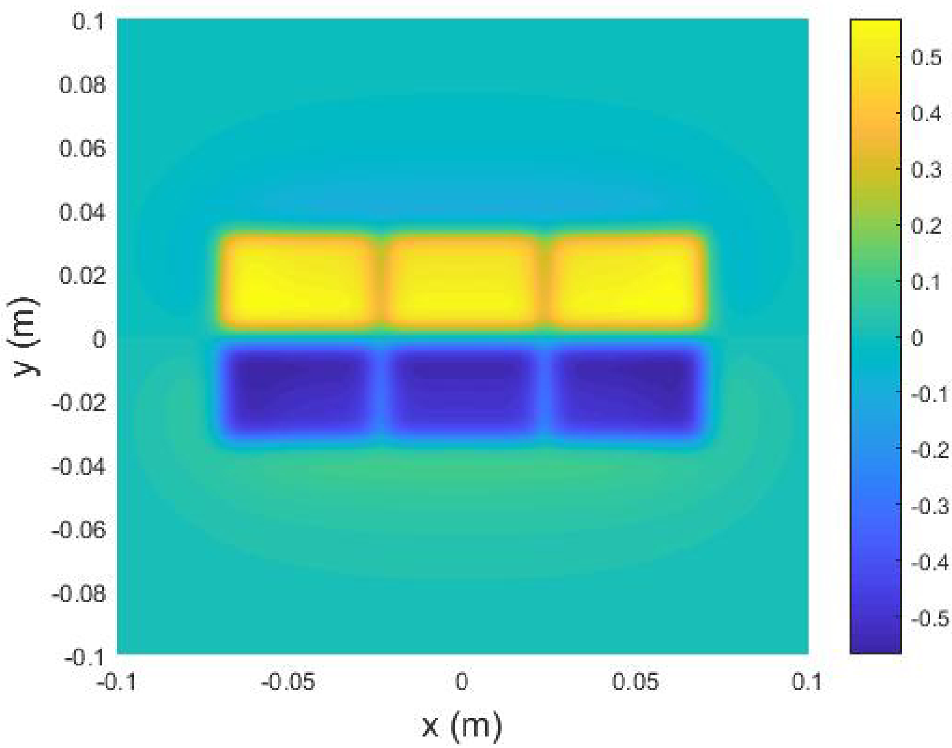

FIG. 15. Map of B_z (in T) in the plane $(0, \boldsymbol{e}_x, \boldsymbol{e}_y)$.

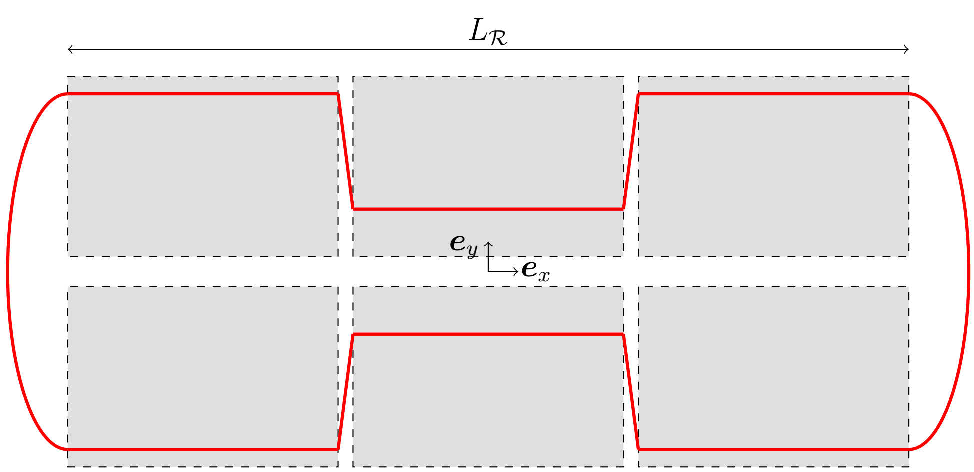

FIG. 16. Example of a loop that maximizes K: The loop is parallel to e_x within the domain $\mathcal{R}$ shown in gray.

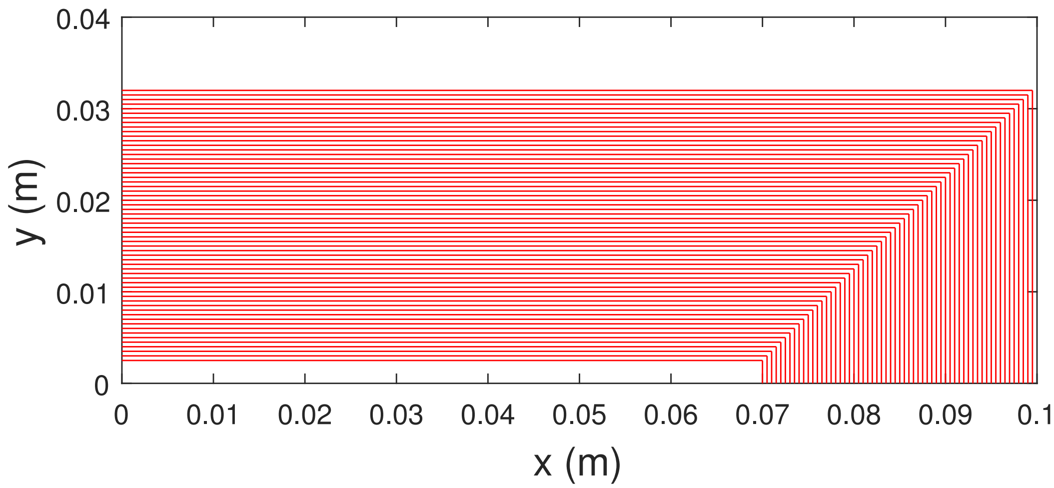

FIG. 17. Optimal coil geometry (only a quarter of the coil is shown).

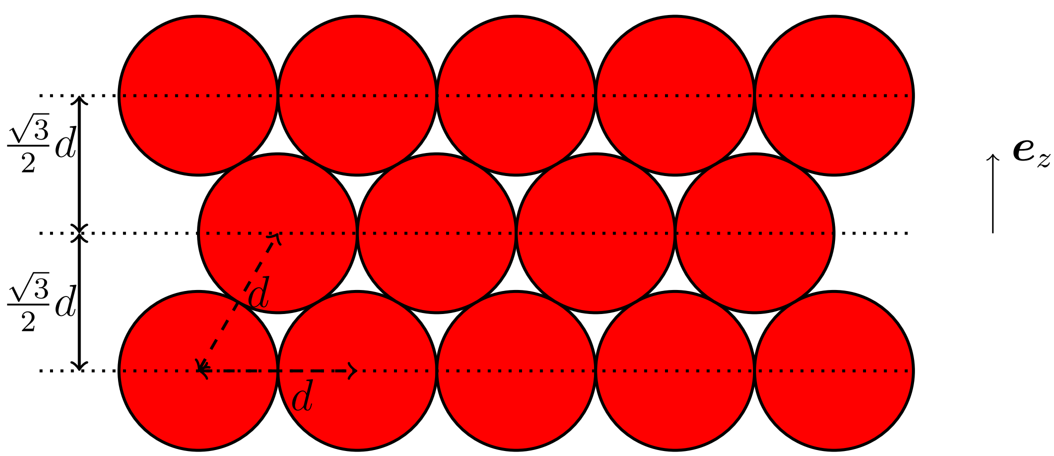

FIG. 18. Cross-section of a compact packing of wires

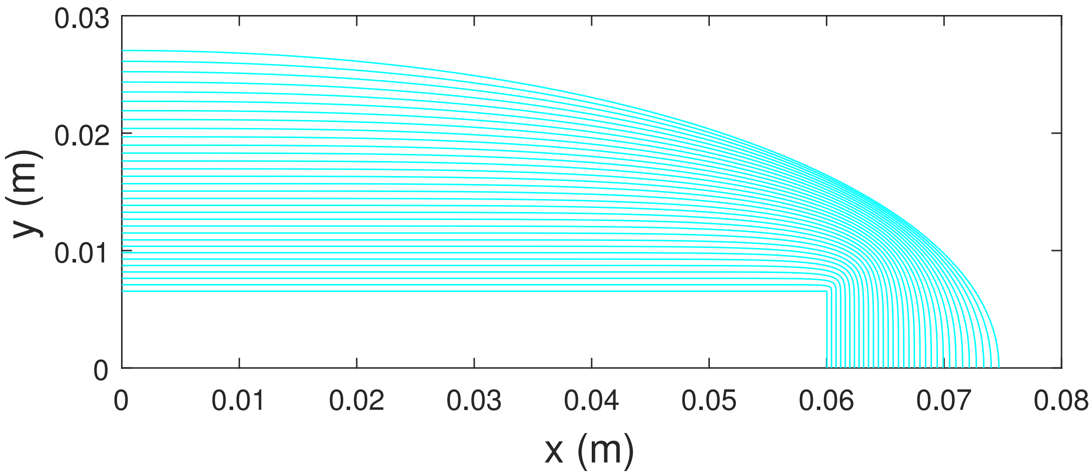

FIG. 19. Model geometry of the designed coil (only a quarter of the coil is shown).

FIG. 20. Laboratory test of the harvester with an harmonic excitation.

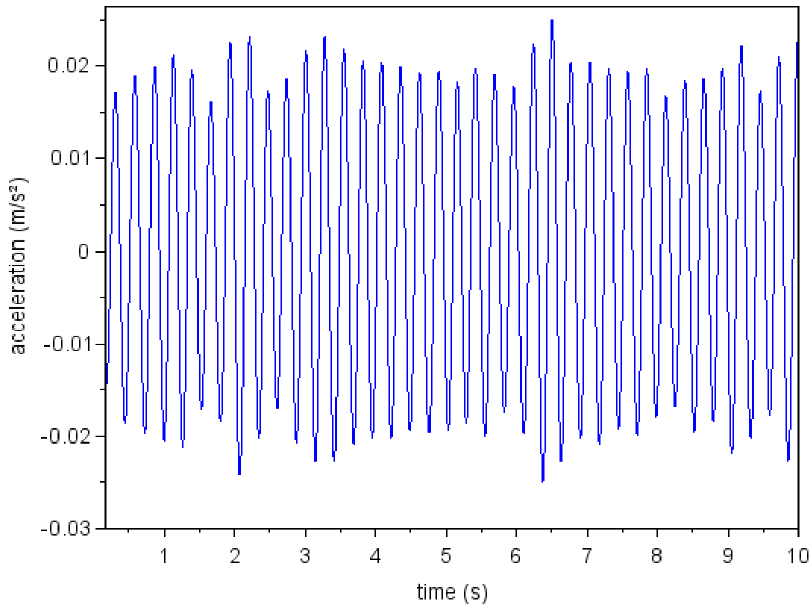

FIG. 21. Base excitation in the laboratory test.

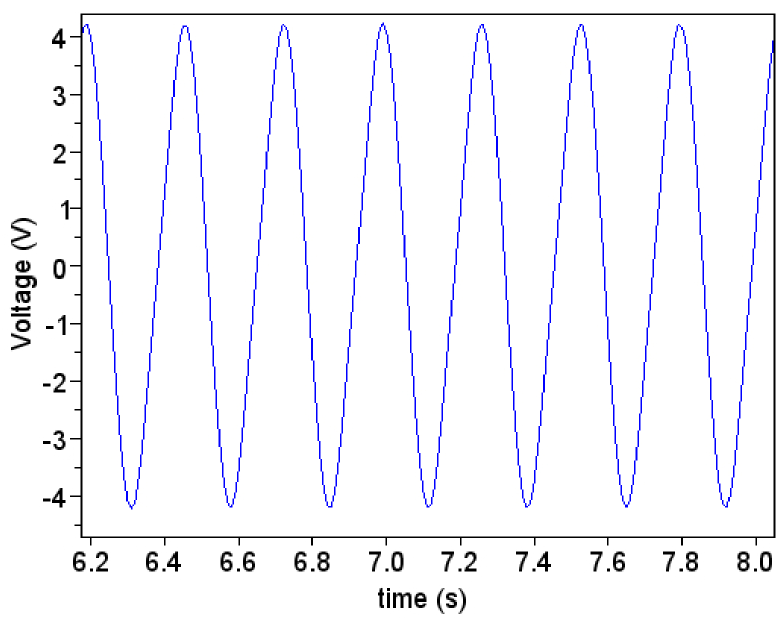

FIG. 22. Voltage measured across the load resistance during the laboratory test.

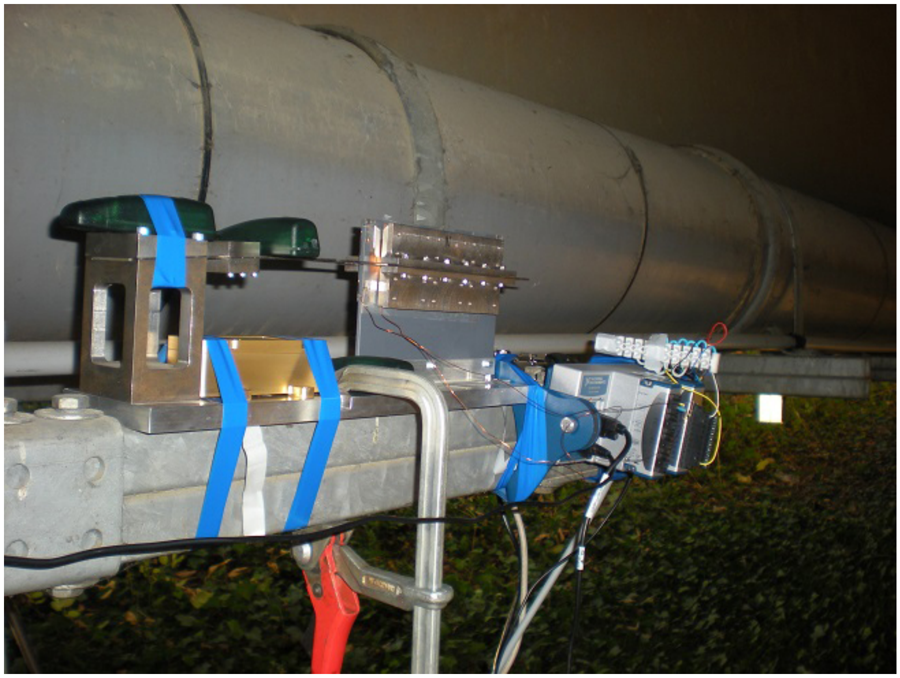

FIG. 23. Setup of the experimental device on the Roberval bridge.

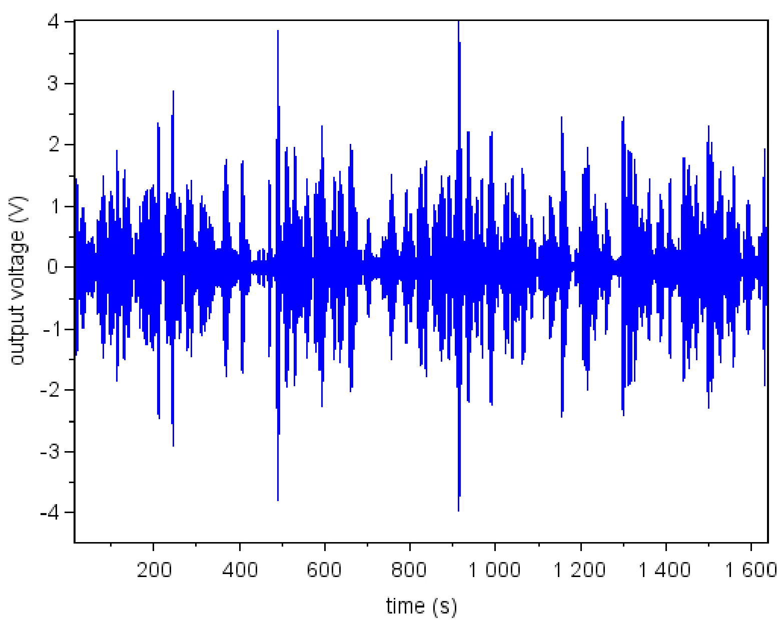

FIG. 24. Voltage measured across the load resistance during field testing.

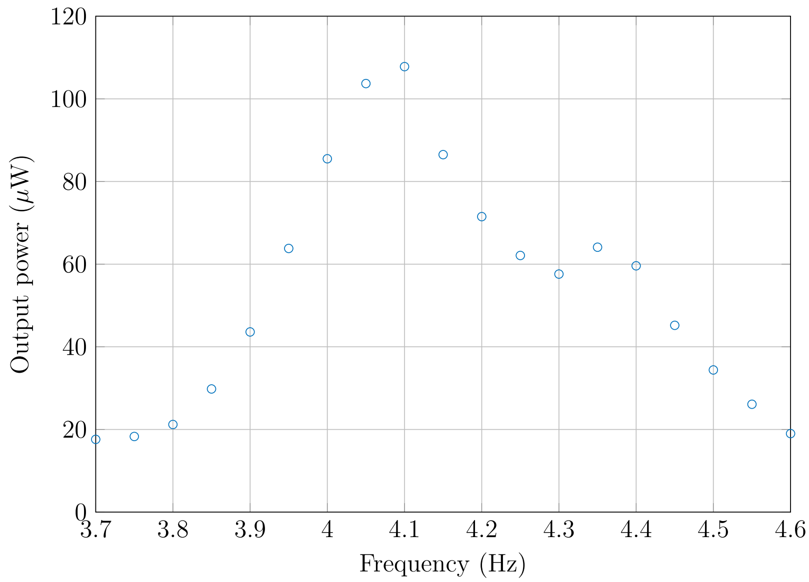

FIG. 25. Mean electrical output power vs oscillator frequency (Roberval bridge).

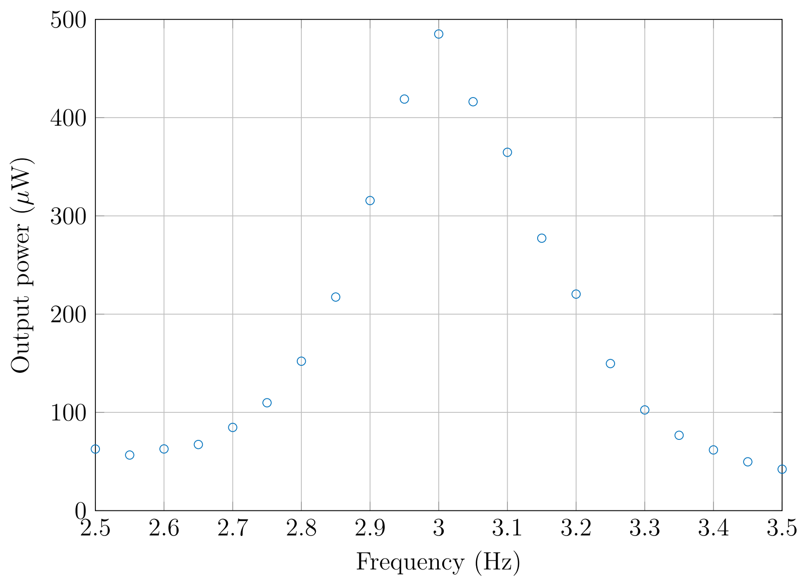

FIG. 26. Mean electrical output power vs oscillator frequency (Vareze bridge).

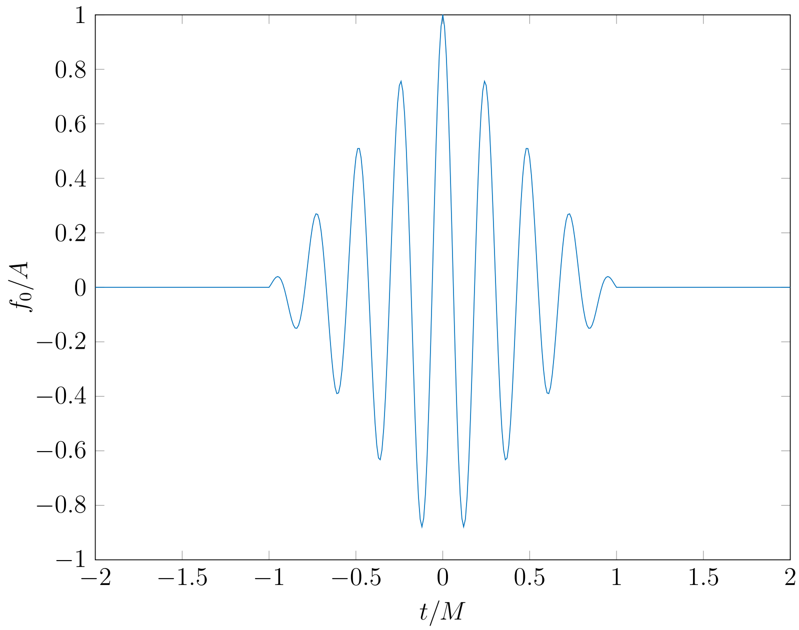

FIG. 27. Pulse model.